Microchemical Journal 227 (2026) 118750

Contents lists available at ScienceDirect

Microchemical Journal

journal homepage: www.elsevier.com/locate/microc

ACEK-integrated capacitive sensing for rapid, label-free quantification of nanoparticles with application to aerosol-exposed droplets

Duygu Yilmaz Aydin [a,b,1], Niloufar Amin [a], Jie Jayne Wu [a,*], Jacob D. Dockery [c], Andrew K. Dickerson [c], Jiangang Chen [d]

[a] Department of Electrical Engineering and Computer Science, The University of Tennessee, Knoxville, TN 7996, USA
[b] Department of Bioengineering, Malatya Turgut Ozal University, 44210, Malatya, Türkiye
[c] Mechanical, Aerospace, and Biomedical Engineering, University of Tennessee, Knoxville, TN 37996-2210, USA
[d] Department of Public Health, The University of Tennessee, Knoxville, TN 37996, USA

ARTICLE INFO

Keywords:
Nanoparticles
Capacitive sensing
AC electrokinetics (ACEK)
Droplet capture

ABSTRACT

Detection of nanoparticles via droplet capture is experimentally challenging, especially at low particle concentrations and small sample volumes. To address this challenge, this study presents an alternating current electrokinetic (ACEK)-integrated interfacial capacitive (AiCap) sensing platform that couples rapid nanofluidic enrichment at interdigitated electrodes with label-free monitoring of interfacial capacitance. Notably, the same applied AC excitation simultaneously drives ACEK transport/enrichment and enables capacitive tracking of nanoparticle adsorption/accumulation at the electrode interface, providing a coupled actuation–readout mechanism. Using 100 nm PSL nanoparticles, excitation conditions were optimized and a calibration was established relating the normalized capacitance change rate to concentration across 10^2 to 10^6 particles/mL. The method achieved a limit of detection (LOD) of 23 particles/mL with a 30 s assay. The sensor was subsequently applied to samples collected from a vertical wind tunnel, where pendant drops were exposed to PSL nanoparticles under controlled airflow conditions to assess nanoparticle scavenging efficiency quantitatively. Together, this work provides a rapid, low-cost workflow for quantifying nanoparticle loading in droplet-based scavenging experiments and for supporting mechanistic studies of droplet–aerosol interactions.

1. Introduction

Nanoparticles are important components of aerosol systems and play a decisive role in environmental processes through radiative interactions, cloud microphysics, and transport processes [1–5]. These particles can influence cloud formation and precipitation dynamics via cloud condensation nuclei as well as radiation scattering and absorption [6–8]. Their presence also has important implications for human health, as they can penetrate deep into the respiratory system and transport harmful chemicals [9–11]. Accurate measurement of nanoparticle concentrations in droplets is therefore essential for mechanistic analysis of droplet–particle interactions and controlled scavenging processes.

While droplet-based scavenging experiments provide controlled insight into particle–droplet interactions, quantitative measurement of nanoparticle concentrations within collected droplets remains difficult due to the small sample volumes and low particle numbers involved [12–14]. Traditional analytical techniques, such as scanning electron microscopy (SEM), transmission electron microscopy (TEM), and dynamic light scattering (DLS), are widely employed for nanoparticle characterization [15,16]. However, these techniques require offline sample collection, extensive preparation, and hours of machine time. Optical counters, such as mass-measurement-type optical particle counting (M-OPC) and light obscuration and dynamic imaging particle counters (LOC & DIPC), are commonly employed for particle detection, but they typically detect particles in the 2–4 μm range but struggle with nanoparticles (<100 nm), often requiring acquisition times exceeding one hour and detection limits of 10^3–10^6 particles/mL [17,18]. A nanopore-based single-particle sensing approach has been reported in which individual nanoparticles are detected through ionic current blockades during translocation across a solid-state nanopore. Using nanopores with diameters on the order of 300 nm, polystyrene nanoparticles in the 100–180 nm size range were successfully detected. By

* Corresponding author.
E-mail address: jaynewu@utk.edu (J.J. Wu).
[1] 0000–0001–5143-9425.

https://doi.org/10.1016/j.microc.2026.118750
Received 28 February 2026; Received in revised form 3 June 2026; Accepted 14 June 2026
Available online 15 June 2026

increasing the electrolyte viscosity up to ~94 mPa·s using water–organic mixtures, nanoparticle translocation times were prolonged from sub-millisecond to millisecond timescales [19]. Advanced methods such as surface-enhanced Raman spectroscopy (SERS), laser-induced breakdown spectroscopy (LIBS), and radiolabel-based assays have been employed to detect nanoparticles like silver, TiO_2 and Polystyrene, but they are constrained by relatively high detection thresholds (typically $\geq 10^5$ particles/mL), long processing times (ranging from 10 min to several hours), and complex instrumentation [20–24]. NTA measurements for 100 nm PSL particles typically require concentrations on the order of $\sim 2 \times 10^7$ particles/mL with acquisition times of approximately 40 s, while LIBD-based detection has been reported at concentrations around $\sim 2 \times 10^6$ particles/mL with analysis times extending to several minutes [25]. Single-particle ICP-MS (spICP-MS) has also been proposed for nanoplastic quantification through metal-assisted labeling strategies. For example, Au-labeled polystyrene nanoplastics were quantified with a reported quantification limit of approximately 8.4 × 105 NPTs/L and a 60 s acquisition time [26]. However, such approaches require nanoparticle labeling and additional sample preparation steps. Py-GC/MS-based approaches have also been investigated for the detection and quantification of nanoplastics through polymer-specific thermal degradation products. These methods provide valuable compositional and quantitative information with high chemical specificity. Despite these advantages, they typically involve multistep analytical workflows and laboratory-scale instrumentation, which may limit their applicability for rapid and on-site nanoparticle analysis [27]. Existing analytical tools often lack the sensitivity, speed, or operational simplicity required to directly quantify nanoparticle loading under these conditions, hindering systematic investigation of scavenging efficiency and removal dynamics. This highlights an urgent need for advanced detection technologies that combine high sensitivity, rapid response, and operational simplicity to effectively monitor nanoparticles in both laboratory and field settings.

Alternating current electrokinetics (ACEK) provides the physical mechanism that enables both nanoparticle manipulation and sensing within this integrated platform. ACEK is a microfluidic technique that manipulates particles and fluids using non-uniform AC electric fields [28–32]. Recent advances in electrokinetic-based sensing technologies, particularly those utilizing ACEK effects, have shown strong potential for real-time, ultra-sensitive detection of nanoparticles in liquid samples [33,34]. In many existing approaches, enrichment and readout are implemented as separate or sequential steps, often requiring additional labeling, fluidic manipulation, or transfer between enrichment and sensing stages. Such multi-step workflows increase system complexity, introduce variability, and reduce suitability for rapid analysis of transient or low-volume samples. To overcome these limitations, we designed a sensor in which electrokinetic enrichment and capacitive detection occur simultaneously at the same electrode interface. Specifically, we develop an alternating current electrokinetics (ACEK)–driven interfacial capacitive sensing platform for rapid, label-free quantification of nanoparticle concentrations in small liquid samples. In this approach, nanoparticles are actively enriched at interdigitated electrode (IDE) surfaces while interfacial capacitance is measured simultaneously using the same AC excitation signal. As nanoparticles adsorb at the electrode–electrolyte interface, they perturb the electrical double layer and interfacial dielectric environment, producing measurable changes in interfacial capacitance that scale with nanoparticle concentration in the solution. By continuously monitoring this capacitance during ACEK-driven enrichment, nanoparticle concentration can be inferred directly from short transient responses, effectively integrating active transport and sensing into a single-step one-pot workflow. This coupled operation distinguishes the present method from approaches that rely on separate enrichment and detection stages, reducing system complexity while enabling rapid quantification at low concentrations.

In this work, 100 nm spherical polystyrene latex (PSL) nanoparticles are employed as model particles to establish quantitative nanoparticle sensing using the ACEK-integrated capacitive sensing platform. A direct quantitative relationship is observed between the normalized capacitance change rate and nanoparticle concentration, enabling rapid quantification with a 30 s assay time and achieving a calculated detection limit of 23 particles mL^{-1}, demonstrating sensitivity suitable for low-volume, low-abundance samples. The sensor is applied to detect PSL nanoparticles scavenged from pendant drops in a vertical wind tunnel, thereby bridging the gap between laboratory calibration and realistic droplet-based aerosol collection experiments. This integrated approach combines the strengths of ACEK-based enrichment and dynamic droplet–aerosol interaction studies, providing a proof-of-concept framework for investigating nanoparticle scavenging and capacitive detection under controlled experimental aerosol conditions. Extension to polydisperse and multi-material aerosol systems may further broaden the applicability of the platform to atmospheric and environmental nanoparticle removal studies. To emphasize the advantages of the developed sensor, Table 1 provides a concise comparison of existing particle detection techniques, summarizing their key performance characteristics.

2. Materials and methods

2.1. Materials and analytical nanoparticle samples

Polystyrene latex (PSL) beads, with a nominal diameter of 100 nm and a stock concentration of 10^9 particles/mL, acetone, isopropyl alcohol (IPA) and phosphate-buffered saline (10×, pH 7.4) were purchased from Thermo Fisher Scientific. PSL nanoparticles are supplied as a stable aqueous dispersion and exhibit hydrophilic interfacial behavior. All reagents were of analytical grade. Serial dilutions of PSL beads were prepared in 0.01× phosphate-buffered saline (PBS), resulting in working solutions with concentrations from 10^2 to 10^6 particles/mL.

2.2. Sensor preparation

Interdigitated electrodes (IDEs) with a multilayer structure comprising copper, nickel, and gold were utilized as the electrode platform in this study. IDEs, as a straightforward and cost-effective platform, have been widely adopted to generate ACEK effects [36,37].

Table 1
A comparative analysis of different techniques for particle detection.

Technology / device	Particle size	LOD	Test time	Ref.
M-OPC	2 μm (PSL)	1.194×10^6 particles/mL	Several hours	[17]
SEM	2 μm (PSL)	1.168×10^6 particles/mL	Several minutes	[17]
LOC & DIPC	4 μm (PSL)	10^3 particles/mL	2 h	[18]
SERS	60 nm (Ag)	10^5 particles/mL	24 min	[21]
NTA	100 nm (PSL)	2×10^7 particles/mL	40 s	[25]
LIBD	100 nm (PSL)	2×10^6 particles/mL	Several minutes	[25]
spICP-MS	135 nm (PSL)	840 particles/mL	60 s	[26]
spICP-MS	60 nm (Au)	212 particles/mL	–	[35]
Radiolabeling	21 nm (TiO_2)	2.5×10^5 particles/mL	5 min	[24]
ACEK (IDE chip)	30 nm and 10 nm (mixed SiO_2/Au)	32 particles/mL	30 s	[33]
ACEK (SAW chip)	50 nm (Cu)	10^2 particles/mL	60 s	[34]
ACEK (SAW chip)	10 nm (SiO_2)	10^4 particles/mL	60 s	[34]
ACEK (IDE chip)	100 nm (PSL)	23 particles/mL	30 s	This work

Each IDE consisted of finger widths and inter-finger gaps of 100 μm. Initially, the surface of the electrodes was mechanically polished using fine polishing pads to ensure a uniform, smooth finish. The electrodes were then subjected to a sequential cleaning protocol, which included rinsing with acetone, followed by IPA, and finally deionized Milli-Q water, ensuring the removal of any surface contaminants. After each rinse step, the electrodes were gently dried under ambient conditions.

A thin gold coating was electroplated onto the surface, ensuring consistent surface conductivity, stability and compatibility with subsequent experiments. Following electroplating, the electrodes underwent an additional cleaning cycle with acetone, IPA, and Milli-Q water to remove any residual plating agents or debris and were again air-dried thoroughly. To enhance surface hydrophilicity and promote uniform droplet spreading during measurements, the electrodes were treated with UV-ozone. Finally, a silicone chamber 2 mm in diameter was carefully attached to the electrode surface, forming a stable well structure for sample holding and analysis.

2.3. Aerosol sample preparation

The samples were prepared by exposing pendant drops to a controlled aerosol stream of PSL nanoparticles within a vertical wind tunnel. PSL nanoparticles were selected as standardized model aerosol particles due to their highly uniform size distribution and well-defined physicochemical properties, which have led to their widespread use as calibration and validation standards in aerosol instrumentation and characterization studies [38–40]. Our experimental setup simulated the scavenging process under realistic airflow conditions. The pendant drops were allowed to interact with the aerosolized PSL particles for a defined period. The system details are provided in the Supplementary Material. After the exposure, the drops were carefully collected and then diluted in 0.01× PBS solution. Before measurement, the samples were treated in an ultrasonic water bath for 30 min to ensure homogenous dispersion of the nanoparticles (Fig. 1), thereby minimizing aggregation and facilitating consistent sensor performance. The resulting suspension was subsequently analyzed using the fabricated ACEK-based sensor.

2.4. Measurement and data processing

Electrical measurements were performed using a precision LCR meter (Keysight® E4980A, Santa Rosa, CA, USA), enabling accurate acquisition of interfacial capacitance under AC excitation (Fig. 1). For each detection trial, 10 μL of the prepared colloidal suspension was dispensed into the silicone chamber mounted over the IDE surface. Following the sample introduction, an AC signal at 10 kHz with an amplitude of 75 mV was applied across the electrodes to induce ACEK effects and facilitate nanoparticle enrichment at the electrode interface.

During the 30 s measurement period, interfacial capacitance (C_{int}) was continuously monitored in real time. The detection strategy is based on the principle that particles collected at the electrode surface alter the local dielectric environment, leading to a measurable change in C_{int}. This capacitive change reflects nanoparticle enrichment and enables label-free, real-time detection of scavenged nanoparticles from pendant droplets. To quantify the sensor response, the normalized capacitance change rate (expressed as dC/dt, %/min) was calculated by performing linear least-squares fitting on the time-dependent normalized capacitance data. To ensure statistical robustness and reproducibility, each sample was tested in three independently fabricated sensors, each used for a single measurement. The results are reported as the mean ± standard deviation of the sensor responses. To minimize potential memory effects associated with residual nanoparticle adsorption and to ensure reproducible interfacial conditions between measurements, each independently fabricated IDE sensor was used for a single measurement. The employed sensing platform is based on low-cost gold-plated PCB interdigitated electrodes, which provide advantages in cost-effectiveness, scalability, and manufacturing reproducibility through standardized large-scale fabrication processes established in the electronics industry. Moreover, PCB-based IDEs can serve as disposable sensors with an average fabrication cost lower than $1 per sensor [37].

3. Sensing mechanism

The sensing performance of the ACEK-integrated capacitive platform

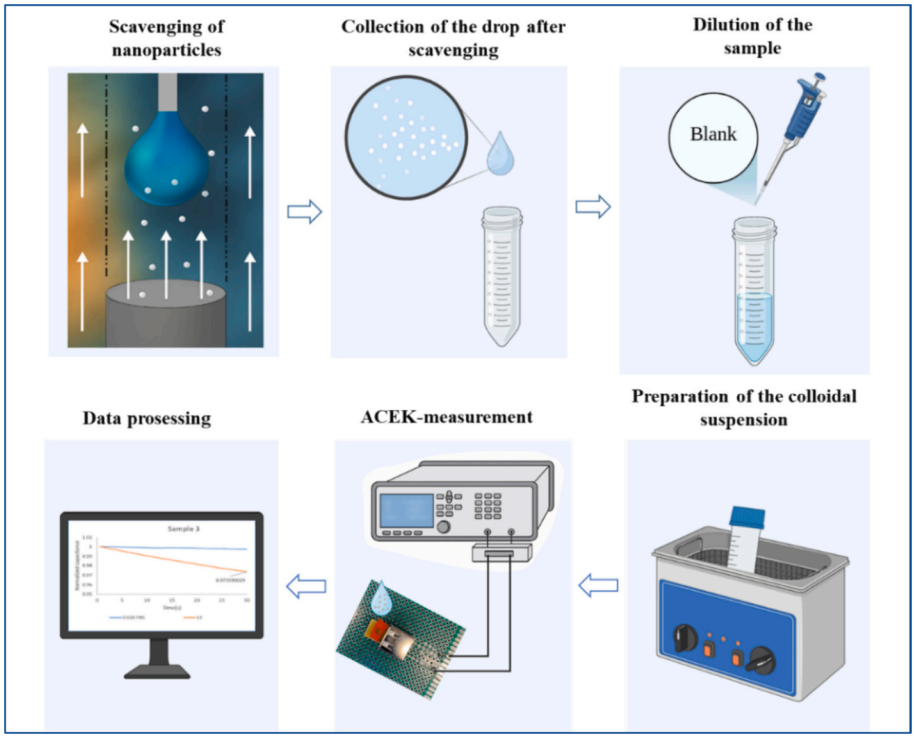

Fig. 1. Experimental procedure of sample preparation and ACEK-integrated capacitive sensing.

arises from the coupling of two key physical processes: modulation of interfacial capacitance at the electrode–electrolyte interface and ACEK-driven nanoparticle enrichment. The following subsections outline the principles of each mechanism and their roles in enabling single-step nanoparticle detection.

3.1. Interfacial capacitance sensing

Interfacial capacitive sensing provides the electrical transduction mechanism by which nanoparticle accumulation at the electrode surface is converted into a measurable signal. Interfacial capacitance sensing is based on monitoring the electric double layer (EDL) formed at the interface between the electrode surface and the surrounding electrolyte solution. When an alternating current (AC) electric field is applied across IDEs, counter-ions in the solution accumulate near the electrode surface, generating an EDL that contributes to the measured C_{int} [33]. EDL formed at the bare electrode surface is illustrated in Fig. 2b, where d_{EDL} represents the thickness of the EDL. Upon exposure to the nanoparticle-containing solution, PSL nanoparticles accumulate at the electrode interface under the applied AC electric field, leading to the formation of an additional dielectric layer, as shown in Fig. 2c. In this case, d_{Np} denotes the effective thickness of the nanoparticle-induced dielectric layer. The accumulation of PSL nanoparticles increases the overall interfacial dielectric layer thickness and alters the local dielectric properties, thereby modulating the capacitance of the sensor.

The interfacial capacitance (C_{int}) is described by:

$$C_{int} = \frac{\varepsilon_s A_{int}}{d_{EDL}}$$

where ε_s is the dielectric permittivity of the solution, A_{int} is the effective surface area of the electrode accessible to the electrolyte, and d_{EDL} is the thickness of the dielectric layer at the interface. As nanoparticles adsorb onto the electrode surface, they can displace the EDL toward the bulk electrolyte, effectively increasing the thickness of the interfacial region and thereby decreasing C_{int}. Following nanoparticle deposition, interfacial capacitance ($C_{int,final}$) can be expressed as:

$$C_{int,final} = \frac{\varepsilon_s A_{int}}{d_{EDL,final}}$$

where $d_{EDL,\ final}$ is the effective surface area of the final capacitor.

To interpret the interfacial capacitance response, an equivalent circuit model of the IDE system is used, as illustrated in Fig. 2c. The complete circuit comprises the dielectric capacitance of the electrode, C_s, and resistive components, including R_{leak} and R_s. Here, R_{leak} represents the leakage resistance at the interface, while R_s denotes the bulk resistance of the electrolyte solution. Under measurement conditions where the influence of R_{leak} and R_s can be considered negligible relative to C_{int}, the circuit simplifies to the right-hand configuration shown in Fig. 2c, where C_{int} *is* connected in series with R_s. This simplified model effectively captures the primary electrical behavior of the IDE system, enabling efficient real-time monitoring of C_{int} during nanoparticle

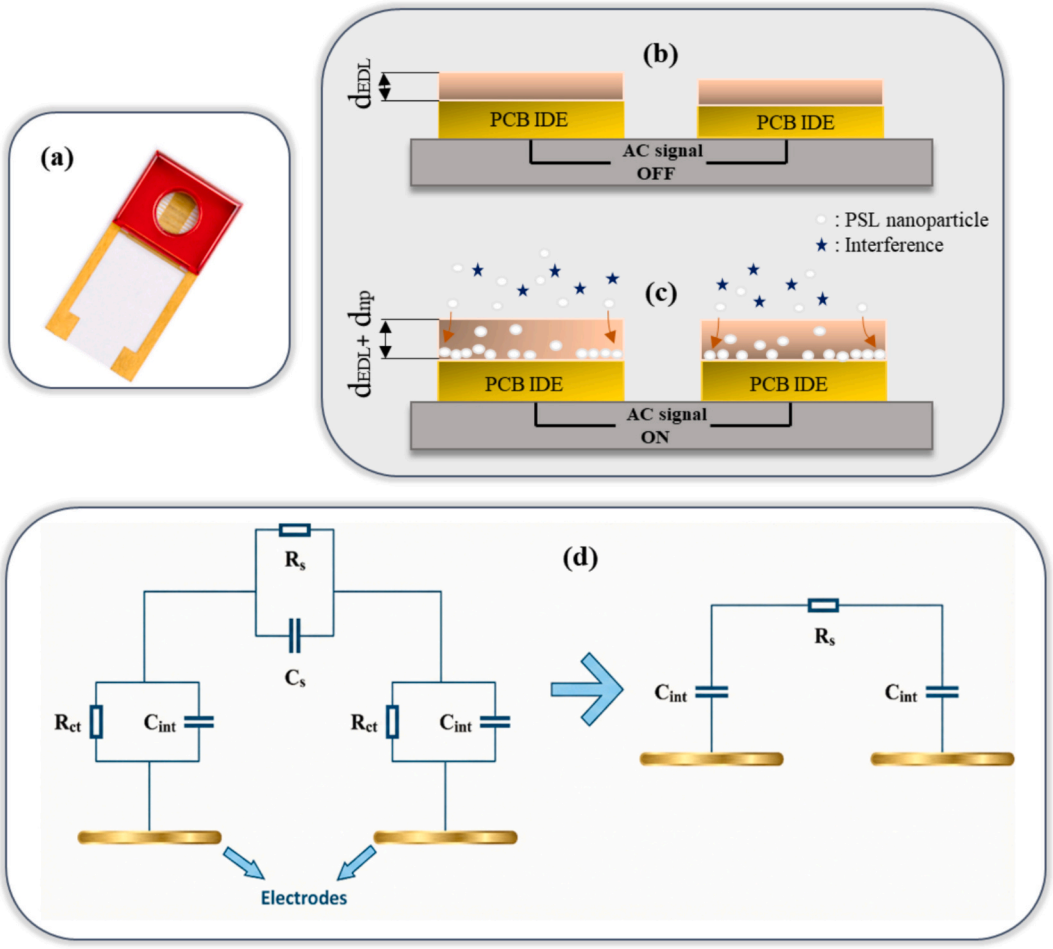

Fig. 2. (a) Printed circuit board interdigitated electrode (PCB IDE). (b) Schematic illustration of the capacitive sensing mechanism based on modulation of the dielectric layer at the bare electrode surface. (c) Modification of the EDL layer thickness due to nanoparticle accumulation at the electrode surface under AC excitation. The orange arrows in EDL represent the DEP force. (d) Equivalent circuit models used for interfacial capacitance measurements. The left side represents the detailed circuit, while the right shows the simplified circuit used for capacitance analysis at the measurement frequency.

detection [41].

This modeling approach provides a quantitative relationship between the measured interfacial capacitance and the dynamic adsorption of nanoparticles at the electrode surface, thus supporting real-time analysis of particle interactions.

3.2. Nanofluidic enrichment of NPs

Alternating current electrokinetics (ACEK) provides the active transport mechanism that drives nanoparticles toward the sensing interface, thereby amplifying interfacial capacitance changes. ACEK includes a range of phenomena, including dielectrophoresis (DEP), AC electroosmosis (ACEO), and AC electrothermal (ACET) flows that can enrich nanoparticles at electrode surfaces by exploiting local electric field gradients [42–46]. These mechanisms significantly improve the sensitivity and speed of detection by increasing the probability of nanoparticle deposition at the sensing interface. DEP arises from the polarization of particles in a non-uniform electric field, resulting in a net force that drives particles toward regions of higher field intensity, particularly near the IDE edges. The DEP-induced velocity of a spherical particle can be expressed as:

$$u_{DEP} \approx \frac{\varepsilon_m a^2 Re[K(\omega)]\nabla|E|^2}{6\eta}$$

where ε_m is the permittivity of the suspending medium, a is the particle radius, $Re[K(\omega)]$ is the real part of the Clausius–Mossotti factor, and $\nabla|E|^2$is the gradient of the square root-mean-square electric field strength, η is the dynamic viscosity of the medium. The electric field lines are enhanced at the edges of the electrodes because of geometric field enhancement. As a result, the spatial variation of $|E|^2$ becomes very sharp. Therefore, the maximum value of $\nabla|E|^2$ occurs at the edges of the electrodes, and the DEP force is larger at the edges than in the gap region. Prior studies have demonstrated that even small DEP forces can locally enrich nanoscale bioparticles and modulate the interfacial capacitance at even low voltages, enabling effective detection using capacitive sensing approaches [47,48].

ACEO refers to the fluid flow induced by the movement of counterions within EDL under the influence of the tangential component of the electric field. This mechanism effectively drags particles toward the electrodes and enhances deposition at the surface. The ACEO velocity (u_{ACEO}) can be estimated as [34]:

$$u_{ACEO} \approx \Lambda \frac{\varepsilon_m V^2}{8\eta r} \frac{\Omega^2}{(1+\Omega^2)^2}$$

where Λ is an empirical coefficient, V is the amplitude of the applied voltage, r is the distance to the center of the gap between adjacent IDE fingers and Ω is a dimensionless frequency parameter dependent on the EDL charging time and electrode geometry. This phenomenon is particularly effective in solutions with low ionic strength and low conductivity, where double-layer formation is stable and strong. ACEO is known to lose efficacy when the solution conductivity exceeds approximately 0.085 S/m [26]. In this study, 0.01× PBS was used, with an electrical conductivity of approximately 0.015 S/m, well within the range where ACEO is expected to operate effectively. Under these conditions, ACEO can contribute to particle enrichment at the electrode surface, complementing other electrokinetic mechanisms.

ACET results from Joule heating of the solution, leading to temperature gradients that induce bulk fluid motion. The ACET velocity (u_{ACET}) can be approximated by [49]:

$$u_{ACET} \approx 5 \text{ X } 10^{-4} \frac{\varepsilon_m \sigma V^4}{k\eta r} \left| \frac{1}{\sigma} \frac{\partial \sigma}{\partial T} \right|$$

where σ is the solution's electrical conductivity, k is the thermal conductivity, and T is the absolute temperature. While ACET effects can play a prominent role in high-conductivity media, at frequencies below a few megahertz, their influence is primarily governed by the applied voltage amplitude rather than frequency [46]. ACET contributions are considered negligible compared to DEP and ACEO, as demonstrated in previous studies [33,34].

The interplay of ACEK mechanisms underpins the enrichment of nanoparticles at the electrode surface in this study. The DEP velocity at the electrode edge was estimated to be 7.4×10^{-8}m/s. Modified PSL nanoparticles can exhibit positive DEP at low to intermediate frequencies in dilute electrolytes due to surface conductance and electrical double-layer polarization, with a crossover to negative DEP at higher frequencies where core permittivity contrast dominates [50]. ACEO velocity was calculated as 1.81×10^{-8}m/s. Decreasing C response may be attributed to ACEO. ACEO weakens as you go into several kHz and above (Supplementary Materials). The ACET-induced velocity was found to be much smaller, on the order of 1.1×10^{-13}m/s. The microflows generated by ACEO make it easier for the convective transport of particles toward the electrodes, which enables local enrichment even at low voltages and conductivities. However, once the particles are close to the electrodes, DEP becomes the dominant force that traps the particles due to polarization in the non-uniform electric field. Given the low-conductivity conditions employed here, ACET effects are expected to remain limited and are not considered the dominant contributor to the enrichment process. This integrated understanding of ACEK effects supports the development of reliable and sensitive detection methods for nanoparticles using interfacial capacitance sensing.

4. Results and discussion

4.1. Optimization of detection parameters

The operational parameters of voltage and frequency influence the balance of electrokinetic phenomena, including DEP and ACEO, that drive nanoparticle enrichment at the electrode interface. Optimizing these conditions is critical to enhancing sensor sensitivity and ensuring reproducible detection in low-conductivity environments. The influence of frequency and voltage on sensor performance was evaluated by measuring the normalized capacitance change rate (dC/dt, %/min), a quantitative indicator of particle accumulation and interfacial changes.

Fig. 3a presents the time-dependent normalized capacitance responses measured over a 30 s interval at different AC frequencies (10–75 kHz) under a voltage of 50 mV at a constant particle concentration of 10^5 particles/mL, and Fig. 3b presents the impact of frequency on the normalized capacitance change rate (dC/dt). At 10 kHz, the sensor exhibited the highest response, with a dC/dt value of −6.24%/min (standard deviation: ±0.1). This result aligns with theoretical expectations that ACEO dominates at low frequencies in low-conductivity solutions (0.01× PBS, conductivity ~0.015 S/m). ACEO induces tangential electric fields that generate microvortices in the electrolyte, effectively convecting nanoparticles toward the electrode surface. As the frequency increased, dC/dt decreased progressively. This trend is consistent with the attenuation of ACEO effects at higher frequencies, where the capacitive reactance of the double layer increases, limiting ion movement and microvortex formation. Although DEP contributions are expected to be relatively weak for nanoparticles at these length scales due to the strong dependence of DEP force on particle volume, frequency-dependent ACEK behavior may still arise from coupled electrokinetic and interfacial polarization effects. Nonetheless, the highest enrichment efficiency observed at 10 kHz highlights the interplay between ACEO-driven convective transport and DEP-assisted trapping at the electrode edges. In aerosol mixtures containing particles with different dielectric properties and sizes, similar bulk interfacial capacitance responses may arise from different particle-loading conditions. Therefore, frequency-dependent ACEK measurements may help improve discrimination between different particle types by exploiting differences in enrichment behavior and interfacial responses across the applied

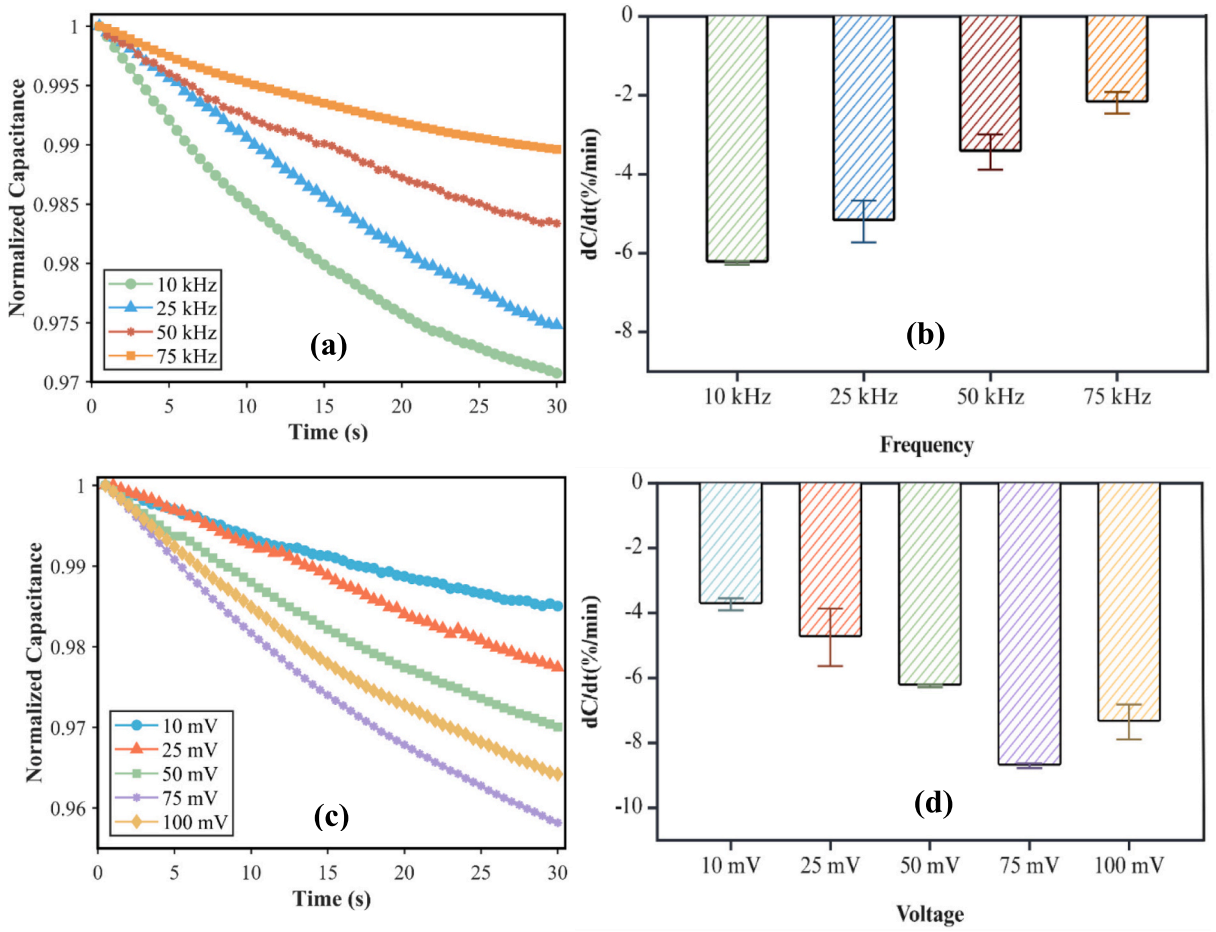

Fig. 3. Frequency and voltage optimization for ACEK-based capacitive sensing of PSL nanoparticles (10^5 particles/mL), assessed through the transient curve and its change rate (dC/dt, %/min). (a) Normalized capacitance versus time at different AC frequencies (10–75 kHz) (b) Effect of AC frequency on the normalized capacitance change rate (dC/dt) at 50 mV, revealing a maximum response at 10 kHz. (c) Normalized capacitance versus time at different voltage amplitudes (10–100 mV) at a fixed frequency of 10 kHz. (d) Dependence of dC/dt on voltage amplitude, highlighting enhanced ACEO-driven enrichment at intermediate voltages, with a maximum observed at 75 mV. Error bars represent the standard deviation of three independent tests.

frequency range.

The normalized capacitance variation as a function of time for different voltages (10 mV–100 mV) at the optimal frequency of 10 kHz and the impact of voltage on the dC/dt are given in Fig. 3c and Fig. 3d, respectively. An increasing trend in dC/dt was observed with rising voltage: $-3.73 \pm 0.18\%$/min at 10 mV, $-4.75 \pm 0.89\%$/min at 25 mV, $-6.24 \pm 0.1\%$/min at 50 mV, and $-8.65 \pm 0.10\%$/min at 75 mV. This behavior can be attributed to the voltage dependence of ACEK phenomena: higher voltages enhance the strength of the tangential electric fields that generate ACEO flows, promoting more efficient particle transport toward the electrode surface. At 100 mV, however, a slight decrease in dC/dt ($-7.35 \pm 0.53\%$/min) was observed. This decline may result from changes in the ACEO-dominated enrichment process under higher electric-field conditions. Because ACEO velocity scales with the square of the applied voltage, stronger electrohydrodynamic flows at elevated voltages may alter near-electrode transport behavior and reduce net particle accumulation efficiency. Additionally, as particles increasingly accumulate at the electrode interface under high-field conditions, electrostatic repulsion and crowding effects may begin to limit further particle deposition, thereby reducing the enrichment observed at 100 mV relative to 75 mV. The observed voltage-dependent behavior underscores the necessity of selecting appropriate AC excitation parameters to maximize ACEO-driven enrichment efficiency while maintaining stable interfacial enrichment conditions. Taken together, the results presented in Fig. 3 demonstrate that optimal nanoparticle enrichment was achieved at 10 kHz and 75 mV under the low-conductivity conditions tested. These operational parameters yielded the most efficient combination of ACEO-induced convective transport and DEP-driven trapping, thereby maximizing sensor response, as reflected in the normalized capacitance change rate.

4.2. *Calibration of sensor response to particle concentration*

The influence of analyte concentration on the sensor response was investigated through real-time interfacial capacitance measurements under optimized conditions. In the experiments, PSL nanoparticle solutions at concentrations ranging from 10^2 to 10^6 particles/mL were introduced to the sensor, and the temporal evolution of normalized capacitance was recorded over a 30 s detection interval (Fig. 4a). As expected, the rate of change of normalized capacitance demonstrated a linear correlation with the PSL nanoparticle concentration, which can be attributed to the enhanced accumulation of nanoparticles at the electrode surface. This trend aligns with the enrichment behavior of the particles driven by AC electrokinetic phenomena, which effectively transport and concentrate analytes at the electrode interface. At a concentration of 10^7 particles/mL, the sensor exhibited a decreased response, suggesting a potential saturation of nanoparticle adsorption at the electrode interface. This phenomenon likely reflects the limited availability of active sites for further particle enrichment under high particle-loading conditions. The surface footprint of a 100 nm PSL

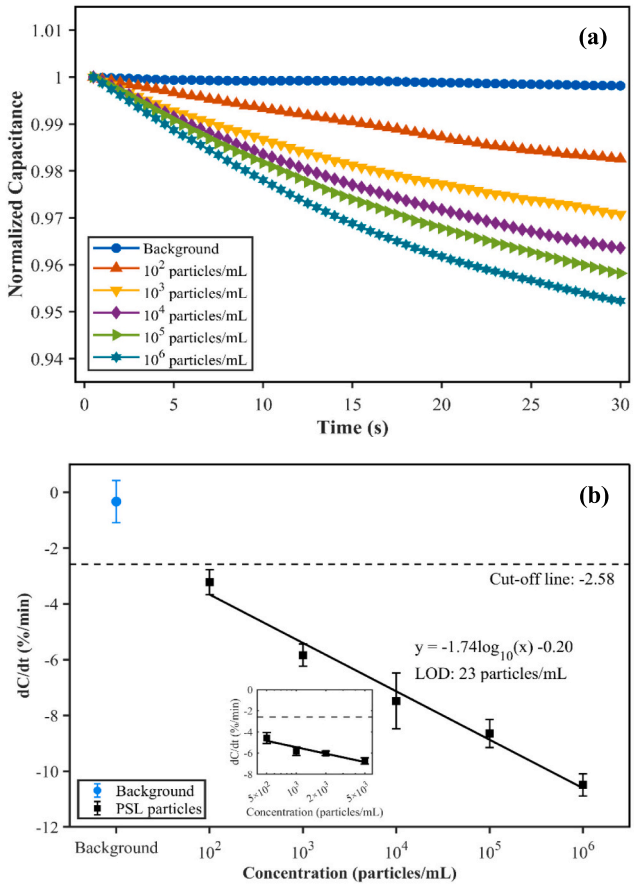

Fig. 4. Concentration-dependent response of the ACEK-based capacitive sensor to PSL nanoparticles. (a) Transient normalized capacitance curves obtained within a 30 s measurement interval. An AC signal of 75 mV at 10 kHz was applied. (b) Sensor response quantified as the rate of normalized capacitance change (dC/dt, %/min). The black symbols represent the response from the PSL sensors, and the control is 0.01× PBS, represented as a blue symbol. (For interpretation of the references to colour in this figure legend, the reader is referred to the web version of this article.)

particle is approximately 7.85 × 10^{-3} μm^2. Although the geometrical IDE surface can theoretically accommodate a large number of particles, ACEK-driven enrichment is primarily localized near electrode-edge high-field regions rather than uniformly distributed across the entire electrode surface. Therefore, progressive occupation of these active regions at high particle concentrations kinetically limits further particle accumulation, leading to a leveling-off of the capacitance response. Mechanistically, this limitation is also coupled with structural changes at the interface. At low-to-moderate nanoparticle concentrations, ACEK-driven enrichment primarily results in relatively uniform near-monolayer accumulation at the electrode interface, enabling a systematic and approximately monotonic relationship between nanoparticle accumulation and interfacial capacitance change. However, at higher particle-loading conditions, progressive nanoparticle accumulation can lead to the formation of more complex interfacial topologies, including clustering, multilayer accumulation, and heterogeneous surface structures. Under these conditions, the electrode–electrolyte interface no longer behaves as a simple uniformly perturbed dielectric layer. Instead, local electric-field distribution, electrical double-layer structure, and interfacial dielectric organization become increasingly heterogeneous, which may disrupt the approximately linear relationship between nanoparticle accumulation and capacitance change. Consequently, the observed decrease in dC/dt at high concentrations is attributed not only to localized enrichment saturation near high-field regions, but also to the evolution of complex nanoparticle interfacial structures that alter the capacitance transduction behavior.

To provide a quantitative assessment of the sensor response, the normalized capacitance change rate (dC/dt, %/min) was calculated for each concentration using linear least-squares regression of the time-dependent normalized capacitance curves (Fig. 4b). The results are summarized as follows: −0.33 ± 0.89%/min (background), −3.22 ± 0.43%/min (10^2 particles/mL), −5.84 ± 0.31%/min (10^3 particles/mL), −7.48 ± 1.03%/min (10^4 particles/mL), −8.65 ± 0.10%/min (10^5 particles/mL), and −10.49 ± 0.40%/min (10^6 particles/mL). As shown in Fig. 4b, a linear relationship was established between dC/dt and the logarithmic PSL nanoparticle concentration (particles/mL), as expressed by the calibration equation: y = −0.20-1.74logx (nanoparticle concentration, particles/mL). The resulting linear relationship, with a correlation coefficient (R^2) of 0.981, demonstrates the sensor's high sensitivity and reliability in quantifying PSL nanoparticles across a wide concentration range (10^2 to 10^6 particles/mL). To determine the sensor's LOD, three times the standard deviation of the background response was used as a cut-off line. This yielded a threshold value of −2.58%/min. By substituting this cut-off into the calibration equation, the LOD was calculated to be 23 particles/mL. This low detection limit highlights the ACEK-enhanced sensor ability to detect ultra-trace levels of PSL nanoparticles with high reproducibility and robustness.

Particle size and shape are known to influence electrokinetic transport and interface deposition; therefore, these parameters can also affect the measured signal magnitude. Nanoparticles with different diameters or non-spherical geometries may exhibit different enrichment efficiencies and surface interaction dynamics near electrode edges, which can alter the response slope and detection sensitivity. While the underlying sensing mechanism remains applicable, extension of the method to particles with different sizes, shapes, or surface chemistries would require system-specific recalibration and parameter optimization [33,34]. In our previous study, the linear detection range for 30 nm SiO_2 nanoparticles was (10^2–10^6) particles/mL, whereas when the particle size decreased to 10 nm, the linear range extended up to 10^7 particles/mL. This behavior can be explained by the ability of smaller particles to occupy a greater number of available adsorption sites on the electrode surface. In addition, the signal response obtained from 30 nm particles was higher than that from 10 nm particles, which is consistent with the fact that DEP velocity is proportional to the particle cross-sectional area [33]. For nanoparticles, electrokinetic behavior is often strongly influenced by surface conductance and electrical double-layer polarization effects due to the large surface-area-to-volume ratio. Under such conditions, the effective dielectric response may become less dependent on bulk material permittivity alone and more governed by interfacial surface properties and particle size. This may partially reduce material-dependent variability in ACEK enrichment behavior for nanoscale particles, which is consistent with the concentration-dependent responses previously observed in mixed nanoparticle systems [33]. In addition, simple pretreatment approaches such as filtration or centrifugation could be employed to roughly fractionate particles by size before sensing, thereby reducing heterogeneity in complex environmental samples.

In complex heterogeneous aerosol mixtures, particles with different sizes and material properties may exhibit distinct frequency-dependent electrokinetic responses. While these material-dependent differences may remain latent or minimized under single-frequency operation because ACEK enrichment is strongly influenced by surface conductance and electrical double-layer polarization effects, they may become more apparent across a broader frequency range because of differences in DEP crossover characteristics and effective particle polarizability. Accordingly, incorporation of multi-frequency ACEK or impedance measurements could provide additional discrimination capability for complex particle systems by exploiting these frequency-dependent dynamics. Furthermore, systematic validation using nanoparticles with different

sizes, dielectric properties, and surface chemistries would provide deeper insight into particle-dependent enrichment dynamics and interfacial capacitance responses. The present platform is primarily developed for rapid quantification of nanoparticle loading under controlled calibration conditions, while improved particle discrimination capabilities will require further investigation.

4.3. Detection of nanoparticles in scavenged droplet samples

The ACEK-based capacitive sensor was used to quantify nanoparticle concentrations in droplets collected after controlled scavenging exposures, applying the previously established calibration relationship to convert capacitance change rates into particle concentrations. This enabled calculation of droplet collection efficiency for different droplet diameters under otherwise consistent exposure conditions. The developed sensing approach links dynamic aerosol–droplet interaction experiments with rapid, label-free nanoparticle quantification in the collected liquid sample. Collection efficiency, *E*, is defined as the ratio of the number of nanoparticles measured in the collected droplet to the number of particles the droplet was exposed to during its residence time in the flow. This quantity depends on droplet cross-sectional area, airflow velocity, exposure time, and aerosol number concentration. In this study, the collection efficiency serves primarily as a practical metric linking the ACEK sensor- measured nanoparticle concentration in the droplet to the controlled exposure conditions in the wind tunnel, rather than as a full characterization of droplet–aerosol interaction physics.

Fig. 5 shows the resulting collection efficiency as a function of pendant drop diameter. A decreasing trend in efficiency is observed as droplet diameter increases from 2.8 to 3.5 mm. The highest collection efficiency is found for the smallest droplet, while larger droplets exhibit reduced collection efficiencies, indicating an inverse relationship between droplet size and aerosol collection performance under the tested conditions. This trend is qualitatively consistent with established wet scavenging theory [51–53], which attributes reduced efficiency at larger droplet sizes to wake formation and flow separation.

Importantly, the agreement between the sensor-derived results and theoretical expectations supports the reliability of the ACEK-based capacitive sensing approach in resolving physically meaningful differences in nanoparticle loading. While a full mechanistic analysis of droplet–flow interactions and electrohydrodynamic effects is beyond the scope of this study, the sensor clearly distinguishes variations in scavenging performance across droplets formed under controlled geometric conditions.

5. Conclusion

In this work, we developed an alternating current electrokinetics (ACEK)–integrated capacitive sensing platform for rapid, label-free quantification of nanoparticle concentrations in small liquid samples. By coupling ACEK-driven enrichment and interfacial capacitance transduction at the same electrode interface, the method enables simultaneous nanoparticle concentration and sensing using a single low-voltage AC excitation. This one-step, one-pot operation eliminates the need for labeling, external preconcentration, or multi-stage fluidic handling, while maintaining a short assay time of 30 s and a calculated detection limit of 23 particles mL^{-1}. Using 100 nm PSL nanoparticles, we established a quantitative relationship between the normalized capacitance change rate and nanoparticle concentration over several orders of magnitude. The platform's performance was further demonstrated through application to droplets collected from pendant-drop scavenging experiments in a controlled wind tunnel. The sensor-resolved collection efficiency trends were qualitatively consistent with theoretical expectations for diffusion-influenced nanoparticle capture, supporting the physical relevance and reliability of the measurement approach in complex, microliter-scale samples.

These results demonstrate the feasibility of ACEK-integrated capacitive sensing for detecting nanoparticles in aerosol-exposed droplet samples without additional labeling or enrichment steps. While this proof-of-concept study used monodisperse PSL particles under controlled experimental conditions, future studies involving polydisperse and multi-component aerosol systems will be important to demonstrate the practical environmental applicability of the proposed platform.

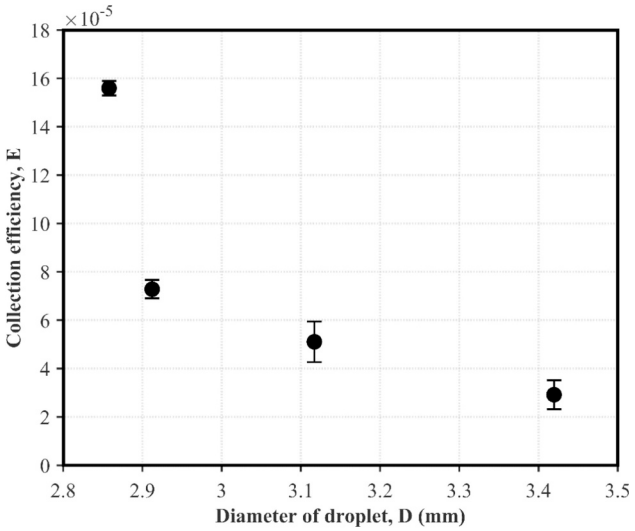

Fig. 5. Collection efficiency is plotted against pendant drop diameter. The measurement of which is made possible by ACEK sensing.

CRediT authorship contribution statement

Duygu Yilmaz Aydin: Writing – review & editing, Writing – original draft, Visualization, Investigation, Formal analysis, Data curation. **Niloufar Amin:** Writing – review & editing, Investigation, Conceptualization. **Jie Jayne Wu:** Writing – review & editing, Writing – original draft, Supervision, Resources, Methodology, Investigation, Conceptualization. **Jacob D. Dockery:** Writing – review & editing, Writing – original draft, Visualization, Formal analysis. **Andrew K. Dickerson:** Writing – review & editing, Resources, Investigation, Funding acquisition. **Jiangang Chen:** Writing – review & editing, Resources, Investigation.

Declaration of competing interest

The authors declare that they have no known competing financial interests or personal relationships that could have appeared to influence the work reported in this paper.

Acknowledgements

We thank the United States Department of Agriculture (Grant No. 2023-67021-40613) and National Science Foundation (Grant No. GEO-2201828) for their support.

Appendix A. Supplementary data

Supplementary data to this article can be found online at https://doi.org/10.1016/j.microc.2026.118750.

Data availability

Data will be made available on request.

References

[1] N.K. Kala, N.S. Anand, M.R. Manoj, H.S. Pathak, K.K. Moorthy, S.K. Satheesh, Zonal variations in the vertical distribution of atmospheric aerosols over the Indian region and the consequent radiative effects, Atmos. Chem. Phys. 22 (9) (2022) 6067–6085, https://doi.org/10.5194/acp-22-6067-2022.

[2] Y. Gao, B. Zhuang, T. Wang, H. Chen, S. Li, W. Wei, H. Lin, M. Li, Climatic–environmental effects of aerosols and their sensitivity to aerosol mixing states in East Asia in winter, Remote Sens. 14 (15) (2022) 3539, https://doi.org/10.3390/rs14153539.

[3] I. Vera-Reyes, E. Vázquez-Núñez, R.H. Lira-Saldivar, B. Méndez-Argüello, Effects of nanoparticles on germination, growth, and plant crop development, in: F. López-Valdez, F. Fernández-Luqueño (Eds.), Agricultural Nanobiotechnology, Springer International Publishing, Cham, 2018, pp. 77–110, https://doi.org/10.1007/978-3-319-96719-6_5.

[4] M.F. Rahim, D. Pal, P.A. Ariya, Physicochemical studies of aerosols at Montreal Trudeau airport: the importance of airborne nanoparticles containing metal contaminants, Environ. Pollut. 246 (2019) 734–744, https://doi.org/10.1016/j.envpol.2018.12.050.

[5] S. Karthick Raja Namasivayam, S. Priyanka, M. Lavanya, S. Krithika Shree, A. L. Francis, G.P. Avinash, R.S. Arvind Bharani, M. Kavisri, M. Moovendhan, A review on vulnerable atmospheric aerosol nanoparticles: sources, impact on the health, ecosystem and management strategies, J. Environ. Manag. 365 (2024) 121644, https://doi.org/10.1016/j.jenvman.2024.121644.

[6] S. Liu, J. Xing, B. Zhao, J. Wang, S. Wang, X. Zhang, A. Ding, Understanding of aerosol–climate interactions in China: aerosol impacts on solar radiation, temperature, cloud, and precipitation and its changes under future climate and emission scenarios, Curr. Pollut. Rep. 5 (2) (2019) 36–51, https://doi.org/10.1007/s40726-019-00107-6.

[7] J.A. Akinyoola, A. Oluleye, I.E. Gbode, A review of atmospheric aerosol impacts on regional extreme weather and climate events, Aerosol Sci. Eng. 8 (3) (2024) 249–274, https://doi.org/10.1007/s41810-024-00223-x.

[8] J. Šesták, P. Hubík, J.J. Mareš, Thermal analysis scheme anticipated for better understanding of the earth climate changes: impact of irradiation, absorbability, atmosphere, and nanoparticles, in: J. Šesták, P. Hubík, J.J. Mareš (Eds.), Thermal Phys. Thermal Anal. 11, Springer International Publishing, Cham, 2017, pp. 471–494, https://doi.org/10.1007/978-3-319-45899-1_22.

[9] M. Sajid, M. Ilyas, C. Basheer, M. Tariq, M. Daud, N. Baig, F. Shehzad, Impact of nanoparticles on human and environment: review of toxicity factors, exposures, control strategies, and future prospects, Environ. Sci. Pollut. Res. 22 (6) (2015) 4122–4143, https://doi.org/10.1007/s11356-014-3994-1.

[10] R. Gupta, H. Xie, Nanoparticles in daily life: applications, toxicity and regulations, J. Environ. Pathol. Toxicol. Oncol. 37 (3) (2018) 209–230, https://doi.org/10.1615/JEnvironPatholToxicolOncol.2018026009.

[11] R.D. Handy, B.J. Shaw, Toxic effects of nanoparticles and nanomaterials: implications for public health, risk assessment and the public perception of nanotechnology, Health Risk Soc. 9 (2) (2007) 125–144, https://doi.org/10.1080/13698570701306807.

[12] Y. Ryu, S. Min, Improving wet and dry deposition of aerosols in WRF-Chem: updates to below-cloud scavenging and coarse-particle dry deposition, J. Adv. Model. Earth Syst. 14 (4) (2022) e2021MS002792, https://doi.org/10.1029/2021MS002792.

[13] C. Blanco-Alegre, A. Castro, A.I. Calvo, F. Oduber, D. Fernández-González, R. M. Valencia-Barrera, A.M. Vega-Maray, T. Molnár, R. Fraile, Towards a model of wet deposition of bioaerosols: the raindrop size role, Sci. Total Environ. 767 (2021) 145426, https://doi.org/10.1016/j.scitotenv.2021.145426.

[14] J.D. Dockery, D.Y. Aydin, A.K. Dickerson, Pendant drop motion and stability in vertical airflow, Phys. Fluids 36 (2) (2024) 027107, https://doi.org/10.1063/5.0187843.

[15] P.S. Kumar, K.G. Pavithra, Mu. Naushad, Characterization techniques for nanomaterials, in: Nanomaterials for Solar Cell Applications, Elsevier, 2019, pp. 97–124, https://doi.org/10.1016/B978-0-12-813337-8.00004-7.

[16] S.K. Brar, M. Verma, Measurement of nanoparticles by light-scattering techniques, TrAC Trends Anal. Chem. 30 (1) (2011) 4–17, https://doi.org/10.1016/j.trac.2010.08.008.

[17] Y. Kuruma, T. Sakaguchi, H. Sakurai, Mass-measurement-type optical particle counting method for determination of number concentration of liquid-borne particles, Adv. Powder Technol. 31 (2) (2020) 848–858, https://doi.org/10.1016/j.apt.2019.12.003.

[18] D.C. Ripple, P.C. DeRose, Primary determination of particle number concentration with light obscuration and dynamic imaging particle counters, J. Res. National Inst. Standards Technol. 123 (2018) 123002, https://doi.org/10.6028/jres.123.002.

[19] T. Kawaguchi, M. Tsutsui, S. Murayama, I.W. Leong, K. Yokota, Y. Komoto, M. Taniguchi, Enhanced nanoparticle sensing in a highly viscous Nanopore, Small Methods 8 (8) (2024) 2301523, https://doi.org/10.1002/smtd.202301523.

[20] H. Guo, B. Xing, L. He, Development of a filter-based method for detecting silver nanoparticles and their Heteroaggregation in aqueous environments by surface-enhanced Raman spectroscopy, Environ. Pollut. 211 (2016) 198–205, https://doi.org/10.1016/j.envpol.2015.12.049.

[21] H. Guo, Z. Zhang, B. Xing, A. Mukherjee, C. Musante, J.C. White, L. He, Analysis of silver nanoparticles in antimicrobial products using surface-enhanced Raman spectroscopy (SERS), Environ. Sci. Technol. 49 (7) (2015) 4317–4324, https://doi.org/10.1021/acs.est.5b00370.

[22] M. Sovago, E.-J. Buis, M. Sandtke, Nanoparticle detection in aqueous solutions using Raman and laser induced breakdown spectroscopy, Spectrochim. Acta B At. Spectrosc. 87 (2013) 182–187, https://doi.org/10.1016/j.sab.2013.05.033.

[23] J. Menneveux, F. Wang, S. Lu, X. Bai, V. Motto-Ros, N. Gilon, Y. Chen, J. Yu, Direct determination of Ti content in sunscreens with laser-induced breakdown spectroscopy: line selection method for high TiO2 nanoparticle concentration, Spectrochim. Acta B At. Spectrosc. 109 (2015) 9–15, https://doi.org/10.1016/j.sab.2015.04.010.

[24] H. Hildebrand, S. Schymura, U. Holzwarth, N. Gibson, M. Dalmiglio, K. Franke, Strategies for radiolabeling of commercial TiO2 nanopowder as a tool for sensitive nanoparticle detection in complex matrices, J. Nanopart. Res. 17 (6) (2015) 278, https://doi.org/10.1007/s11051-015-3080-8.

[25] M.N. Nguyen, P. Lipp, I. Zucker, A.I. Schäfer, Quantification of nanoplastics and inorganic nanoparticles via laser-induced breakdown detection (LIBD), Small Methods 9 (9) (2025) 2402060, https://doi.org/10.1002/smtd.202402060.

[26] J. Jiménez-Lamana, L. Marigliano, J. Allouche, B. Grassl, J. Szpunar, S. Reynaud, A novel strategy for the detection and quantification of nanoplastics by single particle inductively coupled plasma mass spectrometry (ICP-MS), Anal. Chem. 92 (17) (2020) 11664–11672, https://doi.org/10.1021/acs.analchem.0c01536.

[27] G. Dumont, A. Rodrigues, M. Velimirovic, S. Lievens, J. Jordens, J. Focant, P. Stefanuto, Microplastic and nanoplastic analysis: from pyrolysis gas chromatography-mass spectrometry to pyrolysis two-dimensional gas chromatography-mass spectrometry—a critical review, J. Sep. Sci. 48 (10) (2025) e70287, https://doi.org/10.1002/jssc.70287.

[28] Y. Jiang, J. Huang, J. Wu, S. Eda, A rapid, sensitive, and simple-to-use biosensor for on-site detection of Attomolar level microRNA biomarkers from serum extracellular vesicles, Sens. Actuators B 369 (2022) 132314, https://doi.org/10.1016/j.snb.2022.132314.

[29] H. Qi, L. Xiao, J. Wu, L. Lv, X. Hu, Y. Zhuang, X. Liu, W. Zhao, F. You, J. Zhang, L. Zheng, One-step and real-time detection of Hg2+ in brown rice flour using a biosensor integrated with AC electrothermal enrichment, Food Chem. 416 (2023) 135823, https://doi.org/10.1016/j.foodchem.2023.135823.

[30] W. Zheng, J. Chai, J. Wu, J. Zhang, H. Qi, Ultrasensitive and real-time detection of kanamycin residues in milk using an aptasensor based on microfluidic capacitive strategy, Biosensors 15 (5) (2025) 322, https://doi.org/10.3390/bios15050322.

[31] D. Yilmaz Aydin, J.J. Wu, J. Chen, S. Eda, D. Gaddes, L.M. Lee, Rapid and ultra-low detection of cancer biomarker miRNA-133a-3p via AC electrokinetics-integrated capacitive sensing, Microchim. Acta 193 (2) (2026) 109, https://doi.org/10.1007/s00604-026-07844-8.

[32] X. Lin, Y. Jiang, J.J. Wu, S. Eda, N. Wan, An alternating current electrokinetics biosensor for rapid on-site serological screening of Taenia Solium Cysticercosis infection, Microchim. Acta 189 (12) (2022) 476, https://doi.org/10.1007/s00604-022-05575-0.

[33] H. Qi, B. Wang, H. Liang, J.J. Wu, T. Ni, Z. Huang, Y. Lu, J. Zhang, A nanofluidic sensor for real-time detection of ultratrace contaminant particles in IC fabrication, IEEE Sensors J. 21 (1) (2021) 755–764, https://doi.org/10.1109/JSEN.2020.3014011.

[34] J. Zhang, J. Wang, J. Wu, H. Qi, C. Wang, X. Fang, C. Cheng, W. Yang, Rapid detection of ultra-trace nanoparticles based on ACEK enrichment for semiconductor manufacturing quality control, Microfluid. Nanofluid. 23 (1) (2019) 2, https://doi.org/10.1007/s10404-018-2167-9.

[35] E. Goossens, Size detection limits of spICP-MS for analysis of nanoparticles in environmental media, SLU, Dept. of Soil and Environment, 2018.

[36] H. Cui, J. Wu, S. Eda, J. Chen, W. Chen, L. Zheng, Rapid capacitive detection of femtomolar levels of bisphenol a using an aptamer-modified disposable microelectrode array, Microchim. Acta 182 (13–14) (2015) 2361–2367, https://doi.org/10.1007/s00604-015-1556-y.

[37] N. Amin, J. Chen, Q. Cao, H. Qi, J. Zhang, Q. He, J.J. Wu, Low-cost portable sensor for rapid and sensitive detection of Pb2+ ions using capacitance sensing integrated with microfluidic enrichment, Microchim. Acta 191 (11) (2024) 718, https://doi.org/10.1007/s00604-024-06798-z.

[38] C.J. McCrowey, S.S. Tinilau, G. Calderon, J.-E. Koo, D.B. Curtis, A portable high-resolution polar nephelometer for measurement of the angular scattering properties of atmospheric aerosol: design and validation, Aerosol Sci. Technol. 47 (6) (2013) 592–605, https://doi.org/10.1080/02786826.2013.775400.

[39] A. Wiedensohler, W. Birmili, A. Nowak, A. Sonntag, K. Weinhold, M. Merkel, B. Wehner, T. Tuch, S. Pfeifer, et al., Mobility particle size spectrometers: harmonization of technical standards and data structure to facilitate high quality long-term observations of atmospheric particle number size distributions, Atmos. Meas. Tech. 5 (3) (2012) 657–685, https://doi.org/10.5194/amt-5-657-2012.

[40] L. Dong, Y. Han, M. Hu, Y. Zhang, Q. Zhou, Fast atmospheric aerosol size and shape imaging instrument: design, calibration, and intelligent interaction, IEEE Trans. Instrum. Meas. 74 (2025) 1–17, https://doi.org/10.1109/TIM.2025.3551849.

[41] H. Mirzajani, C. Cheng, J. Wu, J. Chen, S. Eda, E. Najafi Aghdam, H. Badri Ghavifekr, A highly sensitive and specific capacitive aptasensor for rapid and label-free trace analysis of bisphenol a (BPA) in canned foods, Biosens. Bioelectron. 89 (2017) 1059–1067, https://doi.org/10.1016/j.bios.2016.09.109.

[42] C. Cheng, J. Wu, E. Fikrig, P. Wang, J. Chen, S. Eda, P. Terry, Unamplified RNA sensor for on-site screening of Zika virus disease in a limited resource setting, ChemElectroChem 4 (3) (2017) 485–489, https://doi.org/10.1002/celc.201600831.

[43] S. Li, H. Cui, Q. Yuan, J. Wu, A. Wadhwa, S. Eda, H. Jiang, AC Electrokinetics-enhanced capacitive immunosensor for point-of-care serodiagnosis of infectious diseases, Biosens. Bioelectron. 51 (2014) 437–443, https://doi.org/10.1016/j.bios.2013.08.016.

[44] M. Lian, N. Islam, J. Wu, AC electrothermal manipulation of conductive fluids and particles for lab-chip applications, IET Nanobiotechnol. 1 (3) (2007) 36–43, https://doi.org/10.1049/iet-nbt:20060022.
[45] C. Cheng, J. Wu, AC electrokinetics-enhanced capacitive virus detection, in: M. Sawan (Ed.), Handbook of Biochips, Springer, New York, New York, NY, 2020, pp. 1–26, https://doi.org/10.1007/978-1-4614-6623-9_40-1.
[46] H. Cui, C. Cheng, X. Lin, J. Wu, J. Chen, S. Eda, Q. Yuan, Rapid and sensitive detection of small biomolecule by capacitive sensing and low field AC electrothermal effect, Sens. Actuators B 226 (2016) 245–253, https://doi.org/10.1016/j.snb.2015.11.129.
[47] S. Li, Q. Yuan, B.I. Morshed, C. Ke, J. Wu, H. Jiang, Dielectrophoretic responses of DNA and fluorophore in physiological solution by impedimetric characterization, Biosens. Bioelectron. 41 (2013) 649–655, https://doi.org/10.1016/j.bios.2012.09.036.
[48] C. Cheng, H. Cui, J. Wu, S. Eda, A PCR-free point-of-care capacitive immunoassay for influenza a virus, Microchim. Acta 184 (6) (2017) 1649–1657, https://doi.org/10.1007/s00604-017-2140-4.
[49] D. Yilmaz Aydin, J.J. Wu, J. Chen, Chiral-dependent redox capacitive biosensor using Cu-Cys-GSH nanoparticles for ultrasensitive H2O2 detection, Biosensors 15 (5) (2025) 315, https://doi.org/10.3390/bios15050315.
[50] M.P. Hughes, Dielectrophoretic behavior of latex nanospheres: low-frequency dispersion, J. Colloid Interface Sci. 250 (2) (2002) 291–294, https://doi.org/10.1006/jcis.2002.8370.
[51] K.-Y. Lai, N. Dayan, M. Kerker, Scavenging of aerosol particles by a falling water drop, J. Atmos. Sci. 35 (4) (1978) 674–682, https://doi.org/10.1175/1520-0469(1978)035%3C0674:SOAPBA%3E2.0.CO;2.
[52] P.K. Wang, H.R. Pruppacher, An experimental determination of the efficiency with which aerosol particles are collected by water drops in subsaturated air, J. Atmos. Sci. 34 (10) (1977) 1664–1669, https://doi.org/10.1175/1520-0469(1977)034%3C1664:AEDOTE%3E2.0.CO;2.
[53] T.S. Pranesha, A.K. Kamra, Scavenging of aerosol particles by large water drops: 1. Neutral case, J. Geophys. Res. Atmos. 101 (D18) (1996) 23373–23380, https://doi.org/10.1029/96JD01311.